Phosphodiester Content Measured in Human Liver by In Vivo ^{31}P MR Spectroscopy at 7 Tesla

Lucian A.B. Purvis,[1]* William T. Clarke,[1] Ladislav Valkovič,[1,2] Christina Levick,[1] Michael Pavlides,[1,3] Eleanor Barnes,[3] Jeremy F. Cobbold,[3] Matthew D. Robson,[1] and Christopher T. Rodgers[1]

Purpose: Phosphorus (^{31}P) metabolites are emerging liver disease biomarkers. Of particular interest are phosphomonoester and phosphodiester (PDE) "peaks" that comprise multiple overlapping resonances in ^{31}P spectra. This study investigates the effect of improved spectral resolution at 7 Tesla (T) on quantifying hepatic metabolites in cirrhosis.

Methods: Five volunteers were scanned to determine metabolite T_1s. Ten volunteers and 11 patients with liver cirrhosis were scanned at 7T. Liver spectra were acquired in 28 min using a 16-channel ^{31}P array and 3D chemical shift imaging. Concentrations were calculated using γ-adenosine-triphosphate (γ-ATP) = 2.65 mmol/L wet tissue.

Results: T_1 means ± standard deviations: phosphatidylcholine 1.05 ± 0.28 s, nicotinamide-adenine-dinucleotide (NAD^+) 2.0 ± 1.0 s, uridine-diphosphoglucose (UDPG) 3.3 ± 1.4 s. Concentrations in healthy volunteers: α-ATP 2.74 ± 0.11 mmol/L wet tissue, inorganic phosphate 2.23 ± 0.20 mmol/L wet tissue, glycerophosphocholine 2.34 ± 0.46 mmol/L wet tissue, glycerophosphoethanolamine 1.50 ± 0.28 mmol/L wet tissue, phosphocholine 1.06 ± 0.16 mmol/L wet tissue, phosphoethanolamine 0.77 ± 0.14 mmol/L wet tissue, NAD^+ 2.37 ± 0.14 mmol/L wet tissue, UDPG 2.00 ± 0.22 mmol/L wet tissue, phosphatidylcholine 1.38 ± 0.31 mmol/L wet tissue. Inorganic phosphate and phosphatidylcholine concentrations were significantly lower in patients; glycerophosphoethanolamine concentrations were significantly higher ($P < 0.05$).

Conclusion: We report human in vivo hepatic T_1s for phosphatidylcholine, NAD^+, and UDPG for the first time at 7T. Our protocol allows high signal-to-noise, repeatable measurement of metabolite concentrations in human liver. The splitting of PDE into its constituent peaks at 7T may allow more insight into changes in metabolism. **Magn Reson Med 78:2095–2105, 2017. © 2017 The Authors Magnetic Resonance in Medicine published by Wiley Periodicals, Inc. on behalf of International Society for Magnetic Resonance in Medicine.**

Key words: ^{31}P; phosphorus; magnetic resonance spectroscopy; human; in vivo; liver; cirrhosis; 7 Tesla

INTRODUCTION

Liver disease is becoming increasingly prevalent (1), now estimated to affect more than 10% of adults in the Europe and America (2). Liver biopsy is the accepted standard test for diagnosis, but biopsy is invasive, can cause pain and bleeding, and has nonnegligible associated mortality (3). In addition, because liver biopsies sample less than 0.0002% of the liver by mass (4), biopsy suffers undesirable sampling variability (5–7). This variability can be seen in studies of paired biopsies for chronic hepatitis C (8,9), and has been blamed for causing "substantial misdiagnosis and staging inaccuracy" in nonalcoholic fatty liver disease (NAFLD) (10).

Phosphorus-31 (^{31}P) metabolites measured using in vivo magnetic resonance spectroscopy (MRS) are emerging biomarkers for several liver diseases including NAFLD (11–13) and cirrhosis (14). The phosphomonoester (PME) and phosphodiester (PDE) peaks of the ^{31}P liver spectrum are particularly promising (15,16). The PME "peak" is believed to contain contributions from phosphocholine (PC) and phosphoethanolamine (PE), which are cell membrane precursors (17). The PDE peak comprises signal from glycerophosphocholine (GPC), and glycerophosphoenthanolamine (GPE), cell membrane degradation products (17). Close to the PDE resonance, there is an overlap of signals from phosphoenolpyruvate (PEP) and, more importantly, from phosphatidylcholine (PtdC), which is a predominant phospholipid component of bile (18–20). At lower field strengths, the spectral resolution needed to individually resolve these five peaks is only possible with ^{1}H decoupling (21,22). This is no longer required at 7T, because the frequency dispersion of peaks increases proportionally to B_0 (18,23). Resolution of individual metabolites can allow more metabolite changes to be visible. For example, PC and PE have been reported at 7T to have opposing changes in human breast cancer, which is not visible in a combined PME peak (24). In the PDE region, there is also a broad baseline resonance from the endoplasmic reticulum (25). In vitro, this resonance broadens from 210 Hz at 1.9 T to 7000 Hz at 7T and shifts

[1]Oxford Centre for Clinical Magnetic Resonance Research (OCMR), University of Oxford, Level 0, John Radcliffe Hospital, Oxford, United Kingdom.
[2]Department of Imaging Methods, Institute of Measurement Science, Slovak Academy of Sciences, Bratislava, Slovakia.
[3]Translational Gastroenterology Unit, University of Oxford, United Kingdom.

Grant sponsor: A Sir Henry Dale Fellowship from the Wellcome Trust and The Royal Society; Grant number: 098436/Z/12/Z.

*Correspondence to: Lucian A.B. Purvis, Oxford Centre for Clinical Magnetic Resonance Research (OCMR), University of Oxford, Level 0, JR Hospital, Oxford, OX3 9DU United Kingdom. E-mail: lucian.purvis@cardiov.ox.ac.uk

Received 14 September 2016; revised 13 January 2017; accepted 17 January 2017

DOI 10.1002/mrm.26635
Published online 28 February 2017 in Wiley Online Library (wileyonlinelibrary.com).

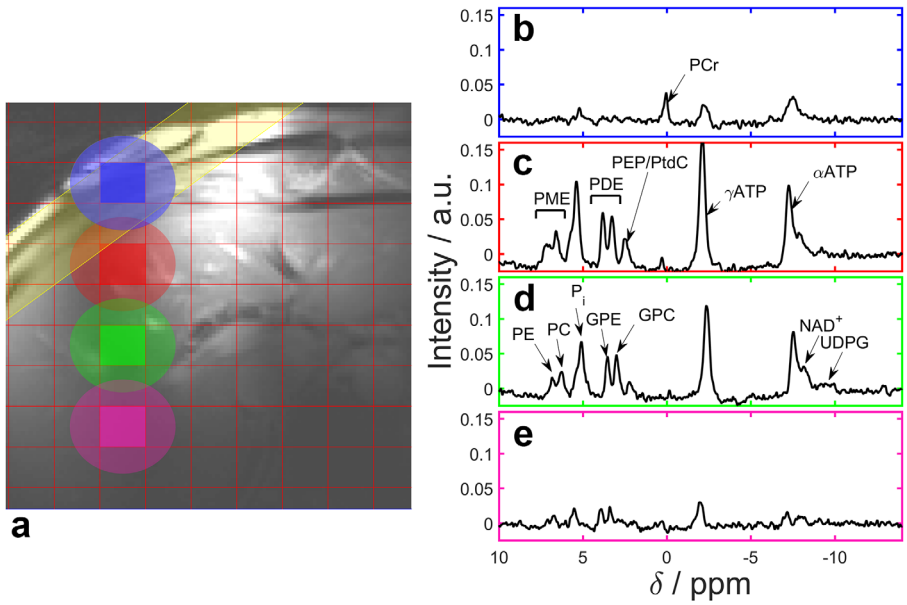

FIG. 1. Typical liver ^{31}P-MRS spectra acquired at 7T in the right lobe of the liver using our 3D UTE-CSI protocol. **a**: The ^{1}H FLASH localizer. The red lines mark the CSI grid, the yellow band marks the outer volume BISTRO suppression. The spectrum for each colored voxel is given on the right side. The ellipses show the extent of the full width at half maximum of the point spread function for each voxel. **b**: A suppressed muscle spectrum taken from the blue voxel. **c–e**: Liver spectra from the red, green and pink voxels, respectively, showing the change as they are taken from deeper in the liver.

toward lower ppm (25). This broadening was observed in vivo in rats at 8.5T (26). We expect these two effects to combine with the inherent increase in the signal-to-noise ratio (SNR) for ^{31}P-MRS at 7T (27) to allow more accurate quantitation of the PME and PDE peaks.

To quantitate these peaks we need to correct for the saturation effects in our CSI protocol and T_1 values must be known. Although there are literature values for most MR-visible ^{31}P liver metabolites at 7T, they do not include PEP/PtdC, nicotinamide adenine dinucleotide (NAD^+), or uridine diphosophoglucose (UDPG). To properly investigate the PDE region, at least the PEP/PtdC T_1 must be known. Therefore, the liver metabolite T_1 values were determined first. The data quality of the normal protocol, including inherent error and repeatability, was then assessed. Finally this protocol was used for quantitation of the PDE region in volunteers and in patients with cirrhotic livers.

METHODS

Patient recruitment to the study was granted ethical approval from the UK National Research Ethics Service (13/SC/0243) and was conducted according to the principles of the 1975 Declaration of Helsinki. All subjects were scanned supine after an overnight fast using an actively shielded whole-body Magnetom 7T (Siemens, Erlangen, Germany).

Transverse, sagittal and coronal ^{1}H fast low angle shot (FLASH) stacks of images for localization, and dual-echo field maps for B_0 shimming were acquired using a 10 cm ^{1}H transmit/receive (Tx/Rx) loop coil (Rapid Biomedical, Germany). B_0 shims were optimized over a region of interest (ROI) covering the entire liver (28). The ^{1}H coil was then replaced with a 16-channel ^{31}P receive array coil (Rapid Biomedical, Germany), consisting of a single $28 \times 27\,cm^2$ transmit loop and a 4×4 matrix of $8 \times 5.5\,cm^2$ diameter flexible receive loops (29). Signal from a spherical phenylphosphonic acid (PPA) fiducial, in housing on the rear of the coil, was acquired using a series of nonlocalized inversion-recovery free induction decays (FIDs) and used to calculate transmit efficiency. Three orthogonal ^{31}P FLASH images were then acquired to localize the fiducial, and used to calculate the coil position (27).

In both T_1 determination and normal protocol, the excitation pulse (a 0.5 ms hard pulse preceded by a numerically optimized portion to flatten the frequency response in a total 2.4 ms duration, described in Rodgers et al) (27) gave a uniform 2000 Hz bandwidth covering all metabolites from UDPG to PC (-9.5 to 7 ppm) (30). The signal was localized using an acquisition-weighted 3D ultrashort echo time chemical shift imaging (UTE-CSI) sequence (31), which uses the shortest possible echo time at each point of k-space. In each case, a B_1-insensitive train to obliterate signal (BISTRO) saturation band was used to suppress overlying skeletal muscle (32) (see Fig. 1). No ^{1}H-decoupling or nuclear Overhauser effect (NOE) enhancement was used.

T_1 Determination

Five male volunteers (28 ± 6 years, body mass index (BMI) $21.3 \pm 2.9\,kg.m^{-2}$) were scanned to determine metabolite T_1 values. A Look-Locker chemical shift imaging (LL-CSI) inversion recovery pulse sequence with 24 effective inversion times (TIs) between 50 ms and 15.55 s was used as previously described (27). Signals were localized to a $6 \times 6 \times 4$ acquisition weighted matrix (interpolated to $8 \times 8 \times 8$ by zero-padding of k-space

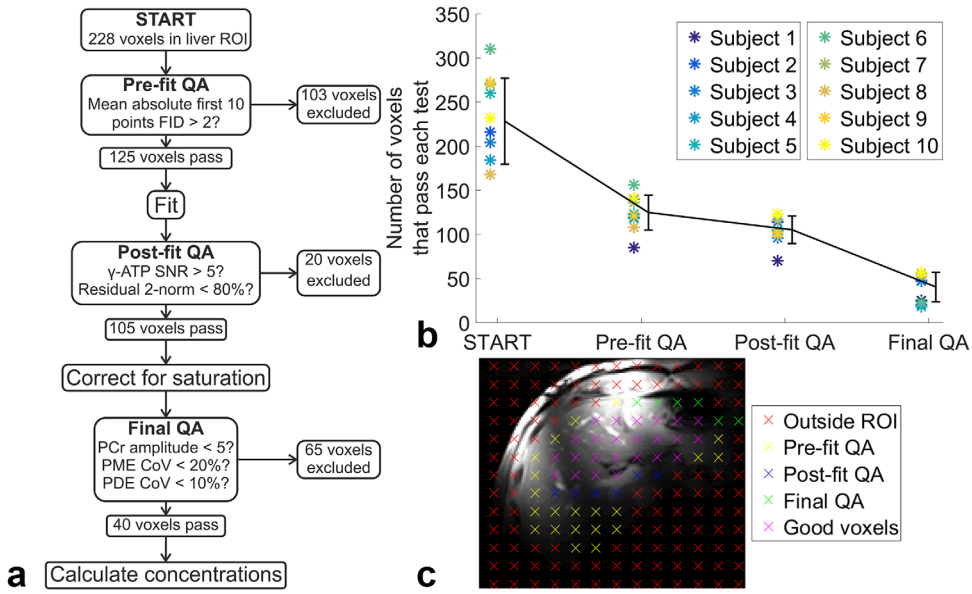

FIG. 2. **a**: The decision tree of quality assurance (QA) tests for excluding voxels in the analysis of the CSI grid of the liver. The mean number of voxels remaining at each step are given. **b**: The number of voxels that pass each test. The black line shows the mean ± SD of the values. The stars show individual values, with each color representing a different subject. **c**: The locations of a single slice of CSI voxels overlaid on a ^{1}H localizer. Each color indicates a different exclusion parameter.

before analysis) and a $200 \times 240 \times 270\,mm^3$ field of view. The LL-CSI sequence was run twice in each subject, first with inversion at +666 Hz [relative to skeletal phosphocreatine (PCr)] and second at -584 Hz (relative to PCr). The inversion pulse bandwidth of 1020 Hz ensured that every metabolite of interest was inverted in at least one data set. One voxel that was fully localized to the liver was manually selected per subject. The following criteria were considered: resolution of the PtdC, PDE and PME regions, skeletal muscle contamination and SNR. Data were fitted to a Bloch simulation of the pulse sequence, as described in the Supporting Information, and the fitting steps are given in Supporting Table S1.

Acquisition

Ten volunteers (six male and four female, 27 ± 5 years; BMI 22.5 ± 1.5 $kg.m^{-2}$) and eleven patients with cirrhosis of the liver (seven male and four female, 61 ± 6 years; BMI 29.5 ± 6.9 $kg.m^{-2}$) were scanned. The patients were recruited based on cirrhosis established using clinical, biochemical or radiological criteria. Five patients had been previously diagnosed with hepatitis C, three with nonalcoholic fatty liver disease, two with alcoholic steatohepatitis, and one with autoimmune hepatitis.

A 1 s T_R, 10 average acquisition-weighted UTE-CSI sequence was used to acquire a $16 \times 16 \times 8$ matrix of liver spectra over a $270 \times 240 \times 200\,mm^3$ field of view in a total acquisition duration of 28 min. To test the repeatability of the protocol, each healthy volunteer was measured a second time in the same session, after full repositioning and reshimming.

Processing

On the scanner, spectra from each receive element were combined with whitened singular value decomposition (WSVD) combination (33,34) to give a single uniform noise spectrum for each voxel.

The full grid of CSI spectra was then loaded into Matlab (MathWorks, Natick, MA). A ROI was manually drawn around the liver on the transverse ^{1}H localizer. Voxels were excluded if they were outside the ROI or if the mean of the absolute of the first 10 points of the FID was less than 2.0 (the noise level in each combined spectrum is scaled by WSVD to be $1/\sqrt{2}$) (33). Each voxel was fitted using a linewidth-constrained, open-source, Matlab spectroscopy fitting tool (35). The additional linewidths were calculated using five 3D CSI datasets acquired from healthy volunteers. The prior knowledge used in the fitting may be found in the Supporting Table S2. After fitting, γ-ATP SNR was calculated as the maximum intensity signal over noise standard deviation (SD) from the spectrum after it had been apodized to match the γ-ATP linewidth. Voxels with γ-ATP SNR less than five, or residual 2-norm greater than 80% of the original were excluded. Saturation correction factors were calculated using the measured T_1 values, accounting for actual flip angle in each voxel calculated from the per-subject B_1 maps computed using Biot-Savart's law (see Supporting Fig. S1, which is available online, for phantom validation) and adjusted for coil loading and position using the PPA FIDs and FLASH images (27). Voxels were discarded if they had PCr amplitude greater than five (i.e. contaminated by skeletal muscle), or a Cramér-Rao lower bound (CRLB), i.e., a measure of the uncertainty in the fit (36), greater than 20% for any PME peak or greater than 10% for any PDE peak. Histograms were used to select the skeletal PCr amplitudes below the normal distribution and PME or PDE CRLB more than two SD above the mean. Any voxels remaining after this automatic quality assurance procedure are referred to below as "high quality". Figure 2a shows the decision tree for exclusion.

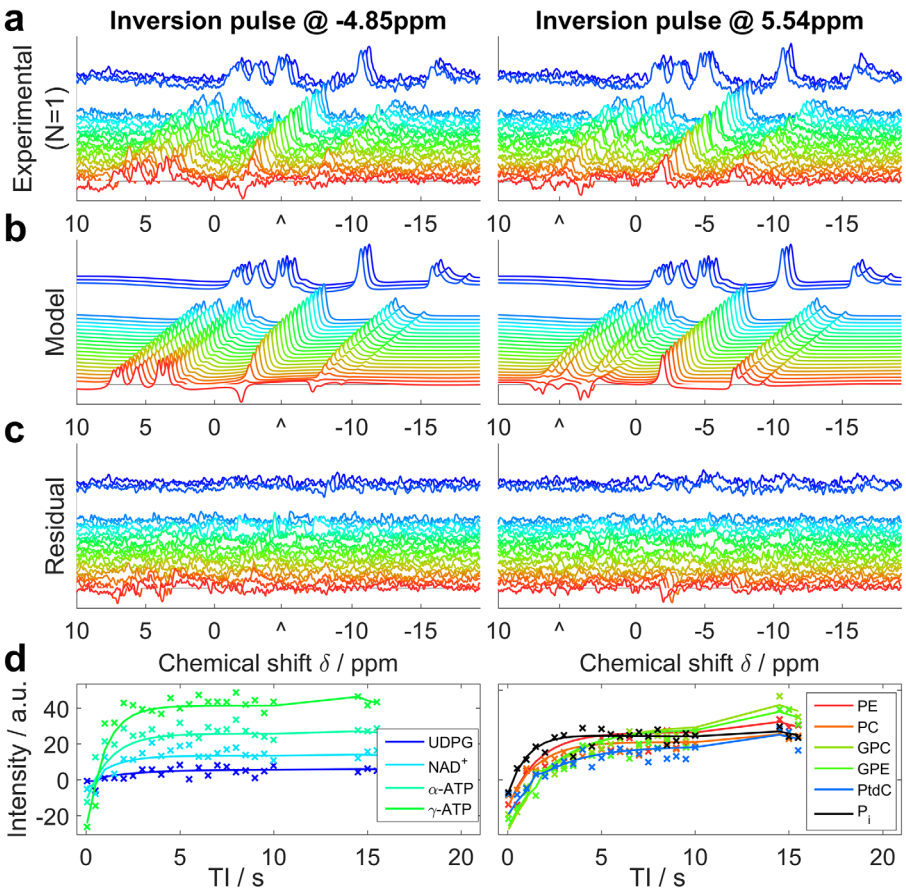

FIG. 3. Illustration of ^{31}P Look-Locker CSI fitting for a typical set of liver data. **a**: Raw spectra from a single voxel of a single subject. Each line shows a different TI, with a gap to indicate the break for magnetization recovery in the pulse sequence. **b**: The model spectra that were fitted simultaneously to the experimental data. **c**: The residual error after fitting. a–c: Images are plotted with the same scaling. "^" marks the central frequency of the inversion pulse. **d**: The absolute intensity sampled at the fitted frequency of each metabolite. Each "x" marks an experimental TI, and the lines show the simulated data. These panels are drawn to help interpret the spectra in a–c, but were not used in the T_1 analysis.

Histograms of the data before and after exclusion were checked manually to ensure that no bias was introduced by using percentage CRLB as exclusion criteria (37).

Concentrations were calculated using γ-ATP as an endogenous reference by assuming that the filling fraction and sensitivities of γ-ATP and each of the other metabolites were equal, and applying Equation [4] from Bottomley (38). The concentration of γ-ATP was taken as 2.65 mmol/L wet tissue based on a 2.51 ± 0.61 mmol/kg wet weight (39), and 1.054 kg/L specific gravity of the liver (40). Metabolites were also quantified as a ratio to the total phosphorus (i.e., the sum of all metabolite peaks). The mean and SD for each subject was calculated from the high quality voxels. The within-subject SDs were calculated using the SDs between the mean values for the repeated volunteer scans, and the coefficients of repeatability (CoRs) were calculated as $1.96 \times \sqrt{2} \times$ the within-subject SD. The mean absolute difference between two repeated scans should be less than the CoR in 95% of cases. For comparison with the CoRs for ^{31}P-MRS from three voxels in the heart at 3T (30), the CoRs were also calculated using the average values from three randomly selected voxels rather than all the available voxels. This was repeated 100 times and the average CoR was used. Bland-Altman plots were used to further analyze the repeatability of the protocol. Welch's t-test was used to compare means, allowing for unequal variances (41). An F-test was used to compare variances.

To calculate the true volume of the CSI voxels, full width at half maximum of the theoretical point spread function (PSF) (42,43) was used in each dimension to form an ellipsoid for each voxel. When several voxels were used, care was taken to count the contribution from overlapping volumes only once.

The liver volume of each subject in mL was approximated by using Equation [1] (from Du Bois and Du Bois) (44) and Equation [2] (from Heinemann et al) (45). This volume was then used to calculate the coverage achieved in this study.

$$\text{Body surface area (BSA)} / \text{m}^2 = 0.007184 \times (\text{mass} / \text{kg})^{0.425} \times (\text{height} / \text{m})^{0.725} \quad [1]$$

$$\text{Liver volume} / \text{mL} = 1072.8 \times (\text{BSA} / \text{m}^2) - 347.5 \quad [2]$$

RESULTS

Figure 1 shows a typical liver spectrum acquired from a volunteer with our standard protocol as described above. The individual PME and PDE peaks are clearly separated. The PEP/PtdC peak is distinct from the GPC peak. The NAD^+ peak is visible on the side of the αATP peak, and there is a small UDPG peak.

An illustration of the T_1 fitting method is given in Figure 3. Healthy human liver metabolite T_1 values are reported and compared with published values in Table 1. The full width half maximum PSF size of a single LL-CSI protocol voxel was 377 mL. The newly determined

Table 1
T_1 Values from Each Subject Are Given with Cramer-Rao Lower Bounds of the Fit[a]

Metabolite	Subject 1	Subject 2	Subject 3	Subject 4	Subject 5	Mean ± SD	Literature values
α-ATP / s	0.66 ± 0.04	0.42 ± 0.04	0.55 ± 0.07	0.62 ± 0.09	0.55 ± 0.05	0.56 ± 0.09	0.46 ± 0.07[b]
γ-ATP / s	0.52 ± 0.03	0.82 ± 0.03	0.62 ± 0.04	0.46 ± 0.04	0.44 ± 0.03	0.57 ± 0.15	0.50 ± 0.08[b]
P_i / s	1.32 ± 0.07	1.40 ± 0.06	1.11 ± 0.09	1.51 ± 0.14	1.34 ± 0.10	1.34 ± 0.15	0.70 ± 0.33[b]
GPC / s	3.5 ± 0.4	3.8 ± 0.3	6.0 ± 3.6	3.7 ± 0.3	2.5 ± 0.3	3.9 ± 1.3	5.94 ± 0.73[b]
GPE / s	4.4 ± 0.3	4.0 ± 0.3	6.2 ± 1.9	3.4 ± 0.4	3.9 ± 0.3	4.4 ± 1.1	6.19 ± 0.91[b]
PC / s	1.5 ± 0.3	2.0 ± 0.2	1.8 ± 0.3	3.1 ± 0.6	2.9 ± 0.7	2.3 ± 0.7	3.74 ± 1.31[b]
PE / s	3.4 ± 0.3	3.9 ± 0.5	4.4 ± 1.0	5.4 ± 0.5	2.4 ± 0.3	3.9 ± 1.1	4.41 ± 1.55[b]
PtdC/ s	1.37 ± 0.25	1.09 ± 0.04	0.70 ± 0.04	1.25 ± 0.17	0.86 ± 0.03	1.05 ± 0.28	0.97 ± 0.30[c]
NAD^+ / s	1.3 ± 0.2	1.6 ± 0.2	1.0 ± 0.3	3.1 ± 0.5	3.2 ± 0.4	2.0 ± 1.0	2.0 ± 1.0[d]
UDPG / s	1.9 ± 0.8	1.9 ± 0.6	3.7 ± 1.3	5.0 ± 1.7	4.0 ± 1.4	3.3 ± 1.4	-

[a]The mean and literature values are given with SD.
[b]7T values from Chmelík et al. (23).
[c]3T value from Bierwagen et al. (20).
[d]1.5T value from Li et al. (21).

T_1 means ± SDs were: PtdC 1.05 ± 0.28 s, NAD^+ 2.0 ± 1.0 s, UDPG 3.3 ± 1.4 s. The T_1 for P_i was 1.34 ± 0.15 s, GPC was 3.9 ± 1.3 s, and GPE was 4.4 ± 1.1 s.

In the main acquisition, an average of 228 ± 49 voxels fell within the ROI, which had a coverage of 92 ± 34%, i.e., approximately the whole liver. 125 ± 20 voxels passed the prefit quality assurance test and 105 ± 16 had a good fit and γ-ATP SNR greater than 5. This left 40 ± 17 high quality voxels, which had good SNR, were well fitted, and were reliably localized to the liver (see Fig. 2).

The nominal voxel size was 6.3 mL, but acquisition weighting means that the 50% maximum point-spread-function volume was 47.1 mL (42,43). The average liver volume was 1.70 ± 0.20 L, and accounting for voxel overlap the average volume within each liver that was analyzed was 0.77 ± 0.17 L. The total liver coverage was, therefore, 46 ± 13%. The mean γ-ATP linewidth is 48 ± 13 Hz, and the average spectral γ-ATP SNR (amplitude / noise SD) was 22 ± 2. The average ratio of the residual PCr signal to ATP was 0.24 ± 0.04 in the liver.

Metabolite concentrations computed for both sets of volunteer scans are given in Table 2. The total PDE concentration measured in healthy volunteers was 3.84 ± 0.68 mmol/L wet tissue, of which 2.34 ± 0.46 mmol/L wet tissue was from GPC and 1.50 ± 0.28 mmol/L wet tissue from GPE. The PtdC/PEP concentration was 1.38 ± 0.31 mmol/L wet tissue.

The Bland-Altman plot for the repeatability scans is shown in Figure 4. The average difference between the two measurements was not significant ($P < 0.1$ for all peaks). The CoRs, CRLB, and inter- and intrasubject SD are given in Table 3. The average γ-ATP CRLB was 1.6%.The PtdC/PEP peak has the largest absolute CoR (55.5%) and the next largest was PE (38.0%). Each of the three-voxel CoRs are significantly larger than the full CoRs ($P < 0.05$ for all peaks).

Average metabolite concentrations for cirrhotic liver are also given in Table 2, and the concentrations for individual patients are given in Table 4 with their diagnoses. The mean total liver volume for cirrhotic liver was 1.76 ± 0.21 L, and the mean volume analyzed in cirrhotic liver was 0.78 ± 0.34 L from 42 ± 23 voxels. The coverage was 46 ± 21%. The average γ-ATP linewidth was 44 ± 19 Hz for patients, and the SNR was 20 ± 6. These are not significantly different from in healthy volunteers. The lowest coverages were 18% for a patient with a BMI of 43.9 $kg.m^{-2}$, and 14.5% for a patient with BMI of 35.6 $kg.m^{-2}$.

Table 2
Mean ± SD of Concentrations for 10 Normal Volunteers and 11 Patients with Cirrhotic Livers from a 28-min 3D CSI Acquisition[a]

Metabolite	Normal liver: Scan 1 / mmol/L wet tissue	Normal liver : Scan 2 / mmol/L wet tissue	Cirrhotic liver / mmol/L wet tissue	Difference between normal (scan 1) and cirrhotic livers/ %	*P*-Value
α-ATP	2.74 ± 0.11	2.69 ± 0.18	2.81 ± 0.11	2.3	0.10
P_i	2.23 ± 0.20	2.18 ± 0.18	1.96 ± 0.23	−12.2	0.005**
GPC	2.34 ± 0.46	2.35 ± 0.48	2.55 ± 0.59	9.1	0.18
GPE	1.50 ± 0.28	1.49 ± 0.21	1.82 ± 0.47	20.9	0.04*
PC	1.06 ± 0.16	0.99 ± 0.17	0.93 ± 0.24	−12.2	0.08
PE	0.77 ± 0.14	0.70 ± 0.11	0.76 ± 0.11	−1.47	0.42
PtdC/PEP	1.38 ± 0.31	1.35 ± 0.38	1.06 ± 0.32	−23.2	0.016*
NAD^+	2.37 ± 0.14	2.33 ± 0.27	2.41 ± 0.38	1.7	0.38
UDPG	2.00 ± 0.22	2.06 ± 0.17	1.99 ± 0.37	−0.6	0.47
PDE	3.84 ± 0.68	3.84 ± 0.66	4.37 ± 0.92	13.7	0.08
PME	1.83 ± 0.27	1.69 ± 0.24	1.69 ± 0.28	−7.7	0.12

[a]The concentrations are based on a 2.65 mmol/L wet tissue γ-ATP concentration. This assumption is reasonable for the normal volunteers, but does not necessarily hold for cirrhosis. The PDE concentration is the sum of the GPC and GPE concentrations, and the PME concentration is the sum of the PC and PE concentrations. Significant differences between healthy and cirrhotic concentrations are marked with stars: * $P < 0.05$, ** $P < 0.01$.

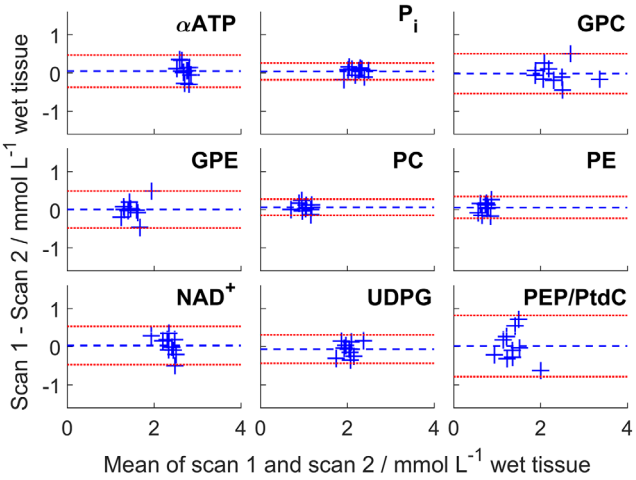

FIG. 4. Bland-Altman plots of the concentrations of the two repeatability scans. Each blue cross marks a different subject. The blue dashed line is the mean difference and the red dashed line is 1.96 × SD, i.e., the 95% confidence interval.

Figure 5 shows the concentrations for each volunteer and patient. There are significant reduction in P_i (12%; $P = 0.005$), and PEP/PtdC concentrations (23%; $P = 0.016$), and a trend to a reduction in PC (12%; $P = 0.08$). There was a significant increase in GPE concentrations (21%; $P = 0.04$). Only NAD^+ has a significantly larger variance in patients than in healthy volunteers (F-test; $P = 0.003$). These differences were also significant when comparing the metabolite ratios to total phosphorus (shown in Supporting Table S3).

DISCUSSION

This study reports T_1 values for PtdC/PEP, NAD^+, and UDPG, which have not previously been measured, as well as the other metabolites visible in ^{31}P spectra. Our main protocol, using CSI localization and a receive array, gave $46 \pm 21\%$ coverage of the liver, while retaining spectra localized to 47.1 mL, which allowed regions of the liver contaminated, e.g., by bile to be excluded. The high average γ-ATP SNR of 20 ± 4 led to low errors in quantitation (γ-ATP CRLB of 1.6%) and there is good spectral resolution of the PME and PDE regions. We have established the error and repeatability in our protocol in ten volunteers. And we have shown that our protocol remains effective in cirrhosis patients, in whom we saw a significant difference in P_i, PEP/PtdC, and GPE compared with volunteers.

T_1 Determination

The 95% confidence intervals of our T_1 values and those in the literature overlapped for all metabolites except for P_i, GPE, and GPC (23). The limited bandwidth of our inversion pulse meant that two inversions were required. Magnetization transfer could, therefore, have reduced the apparent T_1 of the P_i or ATP peaks. However, as the T_1 values were longer than those of Chmelík et al, this effect does not appear to be significant. Chmelík et al performed two IR experiments, one optimized for short T_1 metabolites (eight TI values between 0.02 and 2 s) and the other for long T_1 metabolites (eight TI values between 0.1 and 20 s). The effective TI values in our study (24 between 0.05 s and 15.55 s) are more optimally spaced for intermediate T_1 metabolites. This could be the cause of the differences seen in metabolite T_1 values. Valkovič et al used eight TI values between 0.08 and 3 s, and reported an apparent T_1 of P_i with saturated γ-ATP of 0.77 ± 0.16 s (46). This is consistent with our result (P_i $T_1 = 1.34 \pm 0.15$), as the true T_1 would be longer than the apparent T_1 under saturation.

The three new metabolite T_1 values that we have measured all fall in the intermediate range, and our protocol should, therefore, give an accurate result. Furthermore, previously reported T_1 relaxation times at 1.5T have shown shorter values for ATP, P_i, PME, and PDE in human liver compared with those in calf muscle (47), and a similar effect can be seen at 3T (48,49). Extrapolating to 7T, it could be expected that the average T_1 values for PDE should be shorter than 5.7 ± 1.5 s (49), which is consistent with our findings. Similarly, the T_1 of ATP should be shorter than 1.8 ± 0.1 s (49), and closer to the values seen in the liver at lower field strength (0.4–0.9 s) (21,47,48). It is perhaps surprising that T_1 values in the liver differ so much from those in skeletal muscle and prostate at 7T. Further study will be required to determine the origins of this difference.

Table 3
Coefficients of Repeatability (CoR) in Normals Are Given ± 95% Confidence Intervals[a]

Metabolite	CoR / mmol/L wet tissue	3-Voxel CoR / mmol/L wet tissue	Mean CRLB / mmol/L wet tissue	Mean intrasubject SD (CoV) / mmol/L wet tissue	Intersubject SD (CoV) / mmol/L wet tissue
α-ATP	0.41 (15.1%) ± 0.23	0.83 (30.4%) ± 0.61	0.0269 (1.1%) ± 0.0036	0.45 (16.4%) ± 0.13	0.11 (3.9%)
P_i	0.23 (10.1%) ± 0.08	0.68 (30.3%) ± 0.46	0.0516 (2.3%) ± 0.0047	0.40 (17.9%) ± 0.09	0.20 (8.9%)
GPC	0.50 (21.2%) ± 0.35	1.28 (54.8%) ± 0.88	0.0500 (2.3%) ± 0.0039	0.75 (31.9%) ± 0.17	0.46 (19.5%)
GPE	0.46 (30.5%) ± 0.39	0.84 (55.9%) ± 0.58	0.0386 (2.7%) ± 0.0036	0.47 (31.5%) ± 0.12	0.28 (18.5%)
PC	0.24 (22.9%) ± 0.16	0.74 (69.9%) ± 0.54	0.0431 (4.5%) ± 0.0039	0.46 (43.8%) ± 0.17	0.16 (14.7%)
PE	0.30 (38.9%) ± 0.14	0.65 (84.3%) ± 0.47	0.0376 (5.5%) ± 0.0041	0.37 (48.0%) ± 0.12	0.14 (17.8%)
PtdC	0.76 (55.5%) ± 0.45	1.85 (134.5%) ± 1.59	0.0694 (7.1%) ± 0.0066	0.70 (29.7%) ± 0.14	0.31 (22.7%)
NAD^+	0.48 (20.4%) ± 0.30	1.20 (50.6%) ± 0.80	0.0654 (3.4%) ± 0.0069	0.78 (38.8%) ± 0.14	0.14 (6.0%)
UDPG	0.37 (18.5%) ± 0.20	1.29 (64.6%) ± 0.85	0.0610 (3.8%) ± 0.0063	1.07 (77.8%) ± 0.47	0.22 (10.9%)

[a]The concentrations are based on a 2.65 mmol/L wet tissue γ-ATP concentration, with percentage of peak concentration given in brackets. The intrasubject SDs are reduced compared to fully independent measurements, as there is no correction for voxel overlap.

Table 4
Metabolite Concentrations of 11 Patients with Liver Cirrhosis (Mean ± Intervoxel SD)[a]

Subject	1	2	3	4	5	6	7	8	9	10	11
Diagnosis	HCV	HCV	HCV	HCV	HCV	NAFLD	NAFLD	NAFLD	ASH	ASH	AIH
α-ATP / mmol/L wet tissue	3.04 ± 0.37	2.84 ± 0.24	2.74 ± 0.29	2.69 ± 0.30	2.67 ± 0.31	2.81 ± 0.33	2.92 ± 0.34	2.76 ± 0.31	2.71 ± 0.58	2.77 ± 0.45	2.89 ± 0.40
P_i / mmol/L wet tissue	2.43 ± 0.42	2.14 ± 0.23	1.91 ± 0.31	1.88 ± 0.26	2.09 ± 0.52	1.76 ± 0.22	1.80 ± 0.27	1.67 ± 0.28	1.78 ± 0.22	2.22 ± 0.14	1.85 ± 0.32
GPC / mmol/L wet tissue	1.92 ± 0.64	1.47 ± 0.45	2.78 ± 0.87	2.78 ± 0.71	2.53 ± 1.05	2.09 ± 0.40	2.57 ± 0.70	3.70 ± 1.02	2.93 ± 0.37	2.40 ± 0.41	2.88 ± 0.82
GPE / mmol/L wet tissue	1.94 ± 0.65	0.87 ± 0.29	2.46 ± 0.66	1.57 ± 0.41	1.62 ± 0.59	1.49 ± 0.27	1.55 ± 0.39	1.94 ± 0.60	2.09 ± 0.33	2.48 ± 0.29	1.99 ± 0.58
PC / mmol/L wet tissue	1.18 ± 0.37	1.40 ± 0.41	0.91 ± 0.32	1.21 ± 0.33	0.91 ± 0.51	0.75 ± 0.26	0.82 ± 0.25	0.71 ± 0.24	0.75 ± 0.16	0.94 ± 0.26	0.66 ± 0.27
PE / mmol/L wet tissue	0.83 ± 0.39	0.82 ± 0.35	0.81 ± 0.28	0.59 ± 0.26	0.77 ± 0.34	0.90 ± 0.24	0.59 ± 0.20	0.67 ± 0.31	0.73 ± 0.26	0.92 ± 0.30	0.68 ± 0.36
NAD^+ / mmol/L wet tissue	2.33 ± 0.60	2.49 ± 0.66	2.12 ± 0.65	2.64 ± 0.53	1.98 ± 0.45	3.07 ± 0.49	1.92 ± 0.57	2.40 ± 0.66	2.17 ± 0.50	2.88 ± 0.49	2.55 ± 0.69
UDPG / mmol/L wet tissue	2.15 ± 0.77	1.69 ± 0.69	2.00 ± 0.78	2.44 ± 1.10	1.74 ± 0.73	2.43 ± 0.74	1.53 ± 0.77	2.37 ± 1.00	2.07 ± 0.89	1.37 ± 0.58	2.08 ± 0.91
PEP/PtdC / mmol/L wet tissue	1.37 ± 0.87	1.39 ± 0.91	0.81 ± 0.22	1.35 ± 1.14	1.16 ± 0.58	0.61 ± 0.19	1.37 ± 1.19	0.87 ± 0.39	0.63 ± 0.26	0.79 ± 0.27	1.27 ± 1.38
PDE / mmol/L wet tissue	3.86 ± 1.21	2.35 ± 0.71	5.25 ± 1.49	4.35 ± 1.09	4.14 ± 1.59	3.58 ± 0.65	4.11 ± 1.07	5.65 ± 1.58	5.03 ± 0.68	4.88 ± 0.63	4.87 ± 1.36
PME / mmol/L wet tissue	2.00 ± 0.68	2.21 ± 0.64	1.72 ± 0.55	1.80 ± 0.47	1.67 ± 0.68	1.66 ± 0.33	1.42 ± 0.36	1.38 ± 0.49	1.49 ± 0.25	1.86 ± 0.33	1.34 ± 0.52

[a]Five have been diagnosed with hepatitis C (HCV), three with NAFLD, two with alcoholic steatohepatitis (ASH), and one with auto-immune hepatitis (AIH). The intervoxel SDs are reduced compared to fully independent measurements, as there is no correction for voxel overlap. Intersubject means are given in Table 2.

FIG. 5. A scatter plot of the concentrations of nine different peaks in normal volunteers and patients. Each red "+" marks a subject. The blue line shows the mean ± SD of each group. P_i and PtdC/PEP are significantly lower in cirrhosis than in normal volunteers, and GPE is significantly higher ($P < 0.05$).

Data Quality

Quality assurance in postprocessing is important for CSI methods because the matrix of voxels acquired typically vary widely in SNR, B_o homogeneity and contamination. Automatic methods for the selection of high quality voxels reduce observer bias and the need for postprocessing by experts, and reduce the time required for quality assurance, which is necessary for a protocol to be clinically viable. The trade-off is the possibility of including voxels that would be discarded by an expert. In this study, we checked the performance of the quality assurance pipeline shown in Figure 2 by manual inspection of 100 randomly selected voxels that had been assigned as high quality; all of these voxels had negligible skeletal muscle contamination (PCr) or other artefacts. In healthy volunteers, there was an average PCr/ATP ratio of 0.24 ± 0.04 in liver. As PCr/ATP in skeletal muscle is approximately four, this suggests that skeletal muscle contamination contributes at most 6% of the ATP signal in our "liver" spectra, which is below the noise level in our data.

A single voxel from the CSI grid has a 50% PSF volume of 47.1 mL. Combining the high quality voxels gives an average volume of 0.77 ± 0.17 L. For fully localized 3D-ISIS, voxel sizes have ranged between 75 and 500 mL (11,23,50,51). 3D-CSI, therefore, allows finer spatial resolution across a larger proportion of the liver than previous 3D-ISIS studies, while retaining a feasible scan time. In this study, the finer spatial resolution is used to discard low quality regions and get a more accurate mean value for each subject, under the assumption that the tissue is homogenous in the healthy liver and in diffuse liver disease. The resolution could also be used to investigate heterogeneity in the liver, which is especially useful in focal liver diseases (52).

The mean γ-ATP CRLB in this study was 1.6%. The literature values in the liver at 7T using a 10-cm loop coil are 10.3% for a 20 min 3D-CSI scan and 7.6% for a

3 min 42 s 3D-ISIS scan (23). Accounting for the differences in acquisition time by multiplying by the square root of time, our protocol gives an 82% improvement over the 10-cm loop 3D-CSI scan (23), and a 43.9% improvement over the 10-cm loop 3D-ISIS scan (23). If the difference in volume is also accounted for, the improvements are 70% and 67%, respectively. This can be partly attributed to the difference in postprocessing. The linewidth-constrained fit in the open-source implementation of our fitting tool in Matlab improves the CRLB by including a relationship between the linewidths into the fitting (35). This is particularly important in the PDE/PME region of the spectra, where there are multiple overlapping peaks. Rerunning the analysis using the same prior knowledge as Chmelík et al (23) reduced the number of high quality voxels to 25 ± 10. However, the γ-ATP CRLB of the remaining voxels was 1.65%, i.e., an improvement of 65% over the 10-cm loop CSI scan, and 62% over the ISIS scan. The remaining difference is likely due to increased SNR due to the receive array.

The mean γ-ATP linewidth was 34 ± 11 Hz for the Chmelík et al CSI protocol (23), compared with 48 ± 13 Hz in our protocol. Chmelík et al scanned the subject in a lateral position, and using a double-tuned coil (23). The ^{1}H loop was replaced by the ^{31}P array during our protocol, and so subjects were scanned while supine to ease this coil-swap. Both swapping the coil and scanning supine likely led to the increased linewidths in our protocol ($P < 0.05$). However, the shimming was good enough to allow consistent quantitation of individual PDE peaks.

The average voxel overlap factor of 2.5 was not accounted for when calculating the intrasubject mean and SD. This led to an artificial reduction in the intrasubject SDs given in Tables 3 and 4. Any comparison between the SDs should take this into account.

There were no significant differences between repeated scans. The Bland-Altman plot in Figure 4 shows that there is little variation in most of the metabolite concentrations. It is possible that the small (insignificant) variation observed reflects natural variations in liver metabolite concentrations. Metabolite concentrations in the liver are known to change with nutritional state (53). And although the subjects were scanned after an overnight fast, which should increase the consistency of the results (54), no studies have been reported measuring the consistency of metabolite concentrations in the fasted liver over a long period. The 3 voxel coefficient of repeatability for the ratio of PCr/ATP in the heart at 3T was $1.1/2.14 = 51.4\%$ (30). In comparison, the average liver α-ATP CoR for three voxels randomly selected from the high quality voxels is 30.4%. The coefficient of repeatability is improved by the inclusion of additional voxels, as would be expected.

Metabolite Quantitation at 7T

Our reference concentration of 2.65 mmol/L wet tissue for γ-ATP was chosen based on an ex vivo study (39) that has commonly been used as a reference (55). However, published "absolute quantitation" γ-ATP concentrations have varied widely (1.6 ± 0.3 to 3.8 ± 0.3 mmol/L wet tissue) (21,47,51,56). Any error in the 2.65 mmol/L wet tissue concentration reference will necessarily affect direct comparison with studies performed by absolute concentration methods.

To calculate concentrations using an exogenous reference, knowledge of the B_1^- fields are needed to convert the uniform noise combination of WSVD to a uniform sensitivity combination (34,57). The Biot-Savart method calculates the B_1 at 0 Hz, and could, therefore, be used for the required per-channel B_1^- fields as well as to calculate flip angles. However, the combined transmit and receive magnifies any small errors and so more accurate field maps are required. These were not feasible to acquire in this study. Coil loading must also be accounted for. In this study, we used the signal from a reference fiducial. Alternatively, it would also be possible to use the ERETIC (electronic reference to access in vivo concentrations) method, which uses an electronic reference signal transmitted by a broadband antenna as the calibration reference (58). This is affected by coil loading in the same way as the NMR signal from the body. The advantage of ERETIC is that the signal is already present within the main acquisition, whereas the fiducial method requires running a series of inversion-recovery FIDs.

The variation between centers using exogenous references is greater than the variation within studies at a particular center. It might be possible to resolve these differences in a large multicenter study, but until then each center must be self-referenced (i.e., compare with its own normal values). In that case, relative differences can be detected in the diseased state even when variation between centers exists.

PDE Quantitation in Healthy Volunteers

Despite the feasibility of resolving individual PME and PDE peaks at 3T and below using ^{1}H-decoupling, there has been only one study that has successfully quantified their concentrations separately (21). In other studies either PC/PE or GPC/GPE were not well resolved (51), or only ratios were reported (11,16,22).

The study that achieved quantification used ^{1}H-decoupling, NOE-enhancement, and phospholipid saturation (21). Li et al did not quantify UDPG. The spectra were localized using fully sampled 3D CSI with nominal voxel size of 27 or 64 mL, allowing the quantitation of only a single voxel per subject. They reported significantly larger concentrations for all peaks except PtdC/PEP and PC ($\alpha = 0.05$). However, if their results are scaled to give a γ-ATP concentration of 2.65 mmol/L wet tissue only the GPE concentration is significantly larger in their study ($P = 0.03$), but the NAD^+ and PC concentrations are significantly smaller ($P < 0.0001$).

At 7T, ^{1}H-decoupling, NOE-enhancement and phospholipid saturation is unnecessary to resolve the PDE region, and the added SNR allows better localization with three to ten times smaller voxels than used by Li et al (21).

Although PC and PE are the dominant peaks in the PME region, it is likely that there are other metabolites

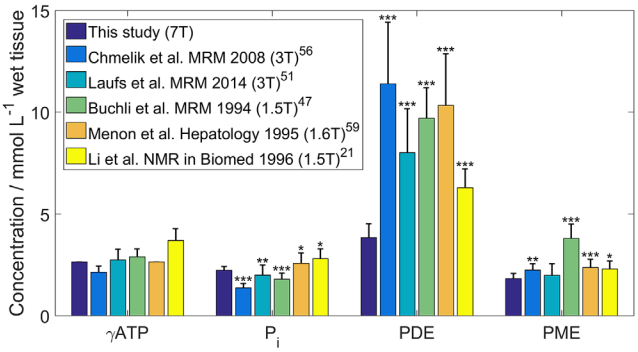

FIG. 6. Comparison of normal liver ^{31}P metabolite concentrations from this study against the literature (21,47,51,56,59). SDs are shown by the error bars on each bar. Stars indicate level of significance of the difference from this study: $^{*}P < 0.05$, $^{**}P < 0.01$, $^{***}P < 0.001$.

in that region (59). It is, therefore, possible that using ^{1}H-decoupling would further enhance quantitation in that region, as well as increasing SNR. However, ^{1}H-decoupling demands high power, and might be limited by safety requirements (60). NOE enhancement is less power intense, and would increase SNR, albeit with the potential of adding variability in metabolite quantitation (60). The use of NOE in this study was prevented by hardware limitations.

By combining the PME and PDE peaks, we can compare our results with more studies. Figure 6 compares the results of this study with five previous studies, one using an endogenous reference (59), and four using an exogenous reference (21,47,51,56). Two studies ran at 3T, one at 1.6T, and two at 1.5T.

The concentration of P_i is significantly larger here than in refs (47,51,56) ($P < 0.01$; Welch's t-test), but significantly smaller than in refs (21,59) ($P < 0.05$). PME is significantly smaller than in refs. (21,47,56,59) ($P < 0.05$), but the difference for PDE is more significant in all cases ($P < 0.0001$, 2.5–7.6 mmol/L wet tissue difference).

At low field strength, it is difficult to distinguish the PEP/PtdC peak from the PDE peak because the peaks strongly overlap (18). But the differences are still significant in the studies where the peaks were quantified separately (18,42).

One possible explanation for this difference is the underlying resonance from endoplasmic reticulum which lies in the same spectral region as PDE. In a direct comparison between 1.5T and 3T, there was a small reduction in the underlying broad peak and a small positive difference between PME/PDE ratios (22). This effect is likely to have become more prominent at 7T, because the endoplasmic reticulum peak will have broadened even further, and may be below the SNR threshold for detection.

In vitro concentrations for GPE (2.59 ± 0.39 mmol/L wet tissue) and GPC (2.48 ± 0.48 mmol/L wet tissue) (61), converted from the published mmol/kg wet weight values using 1.054 kg/L specific gravity (40), match our concentrations more closely than the five in vivo studies we have compared our results with. On the other hand, the PC and PE concentrations measured in the in vitro study were much lower (0.17 ± 0.03 and 0.17 ± 0.04 mmol/L wet tissue) than ours, possibly due to metabolite fluctuations in cold storage which do not affect the PDE peaks (62), but it is also likely that we are including the signal from smaller peaks in the region (61).

Patient Data

The spatial coverage in the patient group was not significantly different than in healthy volunteers. However, as would be expected, patients with very high BMI (e.g., the patient with BMI of 43.9 kg.m^{-2}) allow much lower coverage than the others because the liver is further away from the RF coil. An average γ-ATP linewidth of 43 ± 11 Hz in the patient group indicates that the shim was also not significantly different from in healthy volunteers. Only NAD^+ has a significantly larger variance than in healthy volunteers (F-test; $P = 0.003$), and the residual PCr signal is not significantly higher. Our protocol is, therefore, still effective in patients with cirrhotic livers.

While the concentration of γ-ATP is not expected to change much within a normal population, this might not necessarily be true in patients (63). Therefore, all comparisons of volunteer and patient concentrations should keep the possible differences in γ-ATP concentration between the groups in mind. One reason for a change in ATP concentration might be the presence of fatty infiltrations. This could be addressed in future studies by a lipid partial volume correction.

We saw a significant 12% reduction in P_i ($P = 0.005$), which agrees with the 18% change reported by Dezortova et al in patients with cirrhosis (14). A reduction in P_i has been correlated with an increase in hepatic inflammation (64–66). Dezortova et al also found a significant 34% reduction in PDE, whereas we saw a significant 21% increase in GPE ($P = 0.04$). This difference is partially accounted for by the 23% reduction in PEP/PtdC ($P = 0.02$). Accounting for the effect of Dezortova et al's reported 20% reduction in ATP on the quantification would account for some of this difference, but would also give a significant reduction in the PME concentration, which was not reported by Dezortova et al. The remaining change in PDE, and the increase in PME might be explained by a variation in the underlying phospholipid signal.

CONCLUSIONS

We report for the first time T_1 values for PtdC, NAD^+, and UDPG in human liver at 7T. We used these values to determine a full set of metabolite concentrations in two groups: ten volunteers and eleven patients with cirrhosis. Scanning at 7T enables resolution of the PDE region, without the need for ^{1}H-decoupling. Using a 16-element receive array gives high quality spectra from voxels across the liver. We report comparable quality of data in patients with cirrhosis and in healthy volunteers. 7T ^{31}P spectroscopy with a receive array is a powerful tool for studying metabolism in the diseased liver.

ACKNOWLEDGMENTS

Part of this work has been previously presented at ISMRM (67,68). L.A.B.P. has a DPhil studentship from

the Medical Research Council (UK). We thank Prof Stefan Neubauer for helpful discussion.

REFERENCES

1. Younossi ZM, Stepanova M, Afendy M, Fang Y, Younossi Y, Mir H, Srishord M. Changes in the prevalence of the most common causes of chronic liver diseases in the United States From 1988 to 2008. Clin Gastroenterol Hepatol 2011;9:524–530.e1.
2. Blachier M, Leleu H, Peck-Radosavljevic M, Valla D-C, Roudot-Thoraval F. The burden of liver disease in Europe: a review of available epidemiological data. J Hepatol 2013;58:593–608.
3. Rockey DC, Caldwell SH, Goodman ZD, Nelson RC, Smith AD. Liver biopsy. Hepatology 2009;49:1017–1044.
4. Lee RG. General principles. Diagnostic liver pathology. St. Louis: Mosby-Year Book; 1994. p 1–21.
5. Maharaj B, Leary WP, Naran AD, Maharaj RJ, Cooppan RM, Pirie D, Pudifin DJ. Sampling variability and its influence on the diagnostic yield of percutaneous needle biopsy of the liver. Lancet 1986;327: 523–525.
6. Baunsgaard P, Sanchez GC, Lundborg CJ. The variation of pathological changes in the liver evaluated by double biopsies. Acta Pathol Microbiol Scand A 1979;87:51–57.
7. Abdi W, Millan JC, Mezey E. Sampling variability on percutaneous liver biopsy. Arch Intern Med 1979;139:667–669.
8. Skripenova S, Trainer TD, Krawitt EL, Blaszyk H. Variability of grade and stage in simultaneous paired liver biopsies in patients with hepatitis C. J Clin Pathol 2007;60:321–324.
9. Bedossa P, Dargère D, Paradis V. Sampling variability of liver fibrosis in chronic hepatitis C. Hepatology 2003;38:1449–1457.
10. Ratziu V, Charlotte F, Heurtier A, Gombert S, Giral P, Bruckert E, Grimaldi A, Capron F, Poynard T. Sampling variability of liver biopsy in nonalcoholic fatty liver disease. Gastroenterology 2005;128: 1898–1906.
11. Abrigo JM, Shen J, Wong VWS, Yeung DKW, Wong GLH, Chim AML, Chan AWH, Choi PCL, Chan FKL, Chan HLY, et al. Non-alcoholic fatty liver disease: spectral patterns observed from an in vivo phosphorus magnetic resonance spectroscopy study. J Hepatol 2014;60: 809–815.
12. Valkovič L, Gajdošík M, Traussnigg S, Wolf P, Chmelík M, Kienbacher C, Bogner W, Krebs M, Trauner M, Trattnig S, et al. Application of localized 31P MRS saturation transfer at 7 T for measurement of ATP metabolism in the liver: reproducibility and initial clinical application in patients with non-alcoholic fatty liver disease. Eur Radiol 2014;24:1602–1609.
13. Traussnigg S, Kienbacher C, Gajdosik M, Valkovič L, Hofer H, Ferenci P, Wrba F, Trattnig S, Krssak M, Trauner M. Ultra-high-field MR-spectroscopy in Nafld as non-invasive in-vivo tool for monitoring changes in fat and energy metabolism with potential identification of nash and advanced fibrosis by saturation transfer technique. J Hepatol 2015;62:S739–S740.
14. Dezortova M, Taimr P, Skoch A, Spicak J, Hajek M. Etiology and functional status of liver cirrhosis by 31P MR spectroscopy. World J Gastroenterol 2005;11:6926–6931.
15. Noren B, Dahlqvist O, Lundberg P, Almer S, Kechagias S, Ekstedt M, Franzén L, Wirell S, Smedby Ö. Separation of advanced from mild fibrosis in diffuse liver disease using 31P magnetic resonance spectroscopy. Eur J Radiol 2008;66:313–320.
16. Sevastianova K, Hakkarainen A, Kotronen A, Cornér A, Arkkila P, Arola J, Westerbacka J, Bergholm R, Lundbom J, Lundbom N, et al. Nonalcoholic fatty liver disease: detection of elevated nicotinamide adenine dinucleotide phosphate with in vivo 3.0-T 31P MR spectroscopy with proton decoupling. Radiology 2010;256:466-473.
17. Ruiz-Cabello J, Cohen JS. Phospholipid metabolites as indicators of cancer cell-function. NMR Biomed 1992;5:226–233.
18. Chmelík M, Valkovič L, Wolf P, Bogner W, Gajdošík M, Halilbasic E, Gruber S, Trauner M, Krebs M, Trattnig S, et al. Phosphatidylcholine contributes to in vivo 31P MRS signal from the human liver. Eur Radiol 2015;25:2059–2066.
19. Small DM, Bourges M, Dervichian DG. Ternary and quaternary aqueous systems containing bile salt, lecithin, and cholesterol. Nature 1966;211:816–818.
20. Bierwagen A, Begovatz P, Nowotny P, Markgraf D, Nowotny B, Koliaki C, Giani G, Kluppelholz B, Lundbom J, Roden M. Characterization of the peak at 2.06ppm in P-31 magnetic resonance spectroscopy of human liver: phosphoenolpyruvate or phosphatidylcholine? NMR Biomed 2015;28:898–905.
21. Li CW, Negendank WG, Murphy-Boesch J, Padavic-Shaller K, Brown TR. Molar quantitation of hepatic metabolites in vivo in proton-decoupled, nuclear Overhauser effect enhanced 31P NMR spectra localized by three-dimensional chemical shift imaging. NMR Biomed 1996;9:141–155.
22. Wylezinska M, Cobbold JFL, Fitzpatrick J, McPhail MJW, Crossey MME, Thomas HC, Hajnal JV, Vennart W, Cox IJ, Taylor-Robinson SD. A comparison of single-voxel clinical in vivo hepatic 31P MR spectra acquired at 1.5 and 3.0 Tesla in health and diseased states. NMR Biomed 2011;24:231–237.
23. Chmelík M, Považan M, Krššák M, Gruber S, Tkačov M, Trattnig S, Bogner W. In vivo 31P magnetic resonance spectroscopy of the human liver at 7 T: an initial experience. NMR Biomed 2014;27:478–485.
24. Klomp DWJ, van de Bank BL, Raaijmakers A, Korteweg MA, Possanzini C, Boer VO, de de Berg CA, van de Bosch MA, Luijten PR. (31)P MRSI and (1)H MRS at 7T: initial results in human breast cancer. NMR Biomed 2011;24:1337–1342.
25. Murphy EJ, Bates TE, Williams SR, Watson T, Brindle KM, Rajagopalan B, Radda GK. Endoplasmic-reticulum: the major contributor to the PDE peak in hepatic P-31-NMR spectra at low magnetic-field strengths. Biochim Biophys Acta 1992;1111:51–58.
26. Bates TE, Williams SR, Gadian DG. Phosphodiesters in the liver: the effect of field strength on the 31P signal. Magn Reson Med 1989;12: 145–150.
27. Rodgers CT, Clarke WT, Snyder C, Vaughan JT, Neubauer S, Robson MD. Human cardiac 31P magnetic resonance spectroscopy at 7 tesla. Magn Reson Med 2014;72:304–315.
28. DelaBarre L, Neubauer S, Robson MD, Vaughan JT, Rodgers CT. B_0 shimming further improves human cardiac ^{31}P-MRS at 7 tesla. In Proceedings of the 23rd Annual Meeting of ISMRM, Toronto, Canada, 2015. Abstract 3152.
29. Rodgers CT, Clarke WT, Berthel D, Neubauer S, Robson MD, editors. A 16-element receive array for human cardiac ^{31}P MR spectroscopy at 7T. In Proceedings of the 22nd Annual Meeting of ISMRM, Milan, Italy, 2014. Abstract 2896.
30. Tyler DJ, Emmanuel Y, Cochlin LE, Hudsmith LE, Holloway CJ, Neubauer S, Clarke K, Robson MD. Reproducibility of ^{31}P cardiac magnetic resonance spectroscopy at 3T. NMR Biomed 2009;22: 405–413.
31. Robson MD, Tyler DJ, Neubauer S. Ultrashort TE chemical shift imaging (UTE-CSI). Magn Reson Med 2005;53:267–274.
32. Luo Y, de Graaf RA, DelaBarre L, Tannus A, Garwood M. BISTRO: an outer-volume suppression method that tolerates RF field inhomogeneity. Magn Reson Med 2001;45:1095–1102.
33. Rodgers CT, Robson MD. Receive array magnetic resonance spectroscopy: whitened singular value decomposition (WSVD) gives optimal bayesian solution. Magn Reson Med 2010;63:881–891.
34. Rodgers CT, Robson MD. Coil combination for receive array spectroscopy: are data-driven methods superior to methods using computed field maps? Magn Reson Med 2016;75:473–487.
35. Purvis LAB, Clarke WT, Biasiolli L, Robson MD, Rodgers CT. Linewidth constraints in Matlab AMARES using per-Metabolite T_2 and per-Voxel Delta B_0. In Proceedings of the 22nd Annual Meeting of ISMRM, Milan, Italy, 2014. Abstract 2885.
36. Cavassila S, Deval S, Huegen C, van Ormondt D, Graveron-Demilly D. Cramér-Rao bounds: an evaluation tool for quantitation. NMR Biomed 2001;14:278–283.
37. Kreis R. The trouble with quality filtering based on relative Cramer-Rao lower bounds. Magn Reson Med 2016;75:15–18.
38. Bottomley PA. NMR spectroscopy of the human heart. In: Harris RK, Wasylishen RE, editors. Encyclopaedia of magnetic resonance. Chichester: John Wiley; 2009.
39. Hultman E, von Nilsson LH, Sahlin K. Adenine nucleotide content of human liver normal values and fructose-induced depletion. Scand J Clin Lab Invest 1975;35:245–251.
40. Inai K, Noriki S, Kinoshita K, Nishijima A, Sakai T, Kimura H, Naiki H. Feasibility of liver weight estimation by postmortem computed tomography images: an autopsy study. Pathol Int 2014;64:315–324.
41. Welch BL. The generalizaation of "student's" problem when several different population variances are involved. Biometrika 1947;34:28–35.
42. Pohmann R, von Kienlin M. Accurate phosphorus metabolite images of the human heart by 3D acquisition-weighted CSI. Magn Reson Med 2001;45:817–826.

43. Mareci TH, Brooker HR. Essential considerations for spectral localization using indirect gradient encoding of spatial information. J Magn Reson 1991;92:229–246.
44. Du Bois D, Du Bois EF. Clinical calorimetry: tenth paper a formula to estimate the approximate surface area if height and weight be known. Arch Intern Med 1916;17(6_2):863–71.
45. Heinemann A, Wischhusen F, Püschel K, Rogiers X. Standard liver volume in the caucasian population. Liver Transpl Surg 1999;5: 366–368.
46. Valkovič L, Bogner W, Gajdošík M, Považan M, Kukurová IJ, Kršňák M, Gruber S, Frollo I, Trattnig S, Chmelík M. One-dimensional image-selected in vivo spectroscopy localized phosphorus saturation transfer at 7T. Magn Reson Med 2014;72:1509–1515.
47. Buchli R, Meier D, Martin E, Boesiger P. Assessment of absolute metabolite concentrations in human tissue by 31P MRS in vivo. Part II. Muscle, liver, kidney. Magn Reson Med 1994;32:453–458.
48. Schmid AI, Chmelík M, Szendroedi J, Kršňák M, Brehm A, Moser E, Roden M. Quantitative ATP synthesis in human liver measured by localized 31P spectroscopy using the magnetization transfer experiment. NMR Biomed 2008;21:437–443.
49. Bogner W, Chmelík M, Schmid AI, Moser E, Trattnig S, Gruber S. Assessment of (31)P relaxation times in the human calf muscle: a comparison between 3 T and 7 T in vivo. Magn Reson Med 2009;62: 574–582.
50. Mann DV, Lam WW, Magnus Hjelm N, So NM, Yeung DK, Metreweli C, Lau WY. Biliary drainage for obstructive jaundice enhances hepatic energy status in humans: a 31-phosphorus magnetic resonance spectroscopy study. Gut 2002;50:118–122.
51. Laufs A, Livingstone R, Nowotny B, Nowotny P, Wickrath F, Giani G, Bunke J, Roden M, Hwang J-H. Quantitative liver 31P magnetic resonance spectroscopy at 3T on a clinical scanner. Magn Reson Med 2014;71:1670–1675.
52. Qayyum A. MR Spectroscopy of the liver: principles and clinical applications. radiographics 2009;29:1653–1664.
53. Brinkmann G, Melchert UH, Muhle C, Brossmann J, Link J, Reuter M, Heller M. Influence of different fasting periods on P-31-MR-spectroscopy of the liver in normals and patients with liver metastases. Eur Radiol 1996;6:62–65.
54. Schilling A, Gewiese R, Stiller D, Römer T, Wolf KJ. Einfluß der Ernährungslage auf das 31P-MR-Spektrum der gesunden Leber. Fortschr Röntgenstr 1990;153:369–372.
55. Sijens PE, Dagnelie PC, Halfwerk S, van Dijk P, Wicklow K, Oudkerk M. Understanding the discrepancies between 31P MR spectroscopy assessed liver metabolite concentrations from different institutions. Magn Reson Imaging 1998;16:205–211.
56. Chmelík M, Schmid AI, Gruber S, Szendroedi J, Kršňák M, Trattnig S, Moser E, Roden M. Three-dimensional high-resolution magnetic resonance spectroscopic imaging for absolute quantification of P-31 metabolites in human liver. Magn Reson Med 2008;60:796–802.
57. Roemer PB, Edelstein WA, Hayes CE, Souza SP, Mueller OM. The NMR phased array. Magn Reson Med 1990;16:192–225.
58. Barantin L, LePape A, Akoka S. A new method for absolute quantitation of MRS metabolites. Magn Reson Med 1997;38:179–182.
59. Menon DK, Sargentoni J, Taylor-Robinson SD, Bell JD, Cox IJ, Bryant DJ, Coutts GA, Rolles K, Burroughs AK, Morgan MY. Effect of functional grade and etiology on in vivo hepatic phosphorus-31 magnetic resonance spectroscopy in cirrhosis: biochemical basis of spectral appearances. Hepatology 1995;21:417–427.
60. Lagemaat MW, van de Bank BL, Sati P, Li SZ, Maas MC, Scheenen TWJ. Repeatability of P-31 MRSI in the human brain at 7T with and without the nuclear Overhauser effect. NMR Biomed 2016;29: 256–263.
61. Bell JD, Cox IJ, Sargentoni J, Peden CJ, Menon DK, Foster CS, Watanapa P, Iles RA, Urenjak J. A P-31 and H-1-NMR investigation in-vitro of normal and abnormal human liver. Biochim Biophys Acta 1993;1225:71–77.
62. Changani KK, Fuller BJ, Bell JD, Taylor-Robinson SD, Moore DP, Davidson BR. Improved preservation solutions for organ storage - a dynamic study of hepatic metabolism. Transplantation 1999;68:345–355.
63. Szendroedi J, Chmelík M, Schmid AI, Nowotny P, Brehm A, Kršňák M, Moser E, Roden M. Abnormal hepatic energy homeostasis in type 2 diabetes. Hepatology 2009;50:1079–1086.
64. Jalan R, Sargentoni J, Coutts GA, Bell JD, Rolles K, Burroughs AK, Taylor Robinson SD. Hepatic phosphorus-31 magnetic resonance spectroscopy in primary biliary cirrhosis and its relation to prognostic models. Gut 1996;39:141–146.
65. Taylor-Robinson SD, Sargentoni J, Bell JD, Thomas EL, Marcus CD, Changani KK, Saeed N, Hodgson HJF, Davidson BR, Burroughs AK, et al. In vivo and in vitro hepatic phosphorus-31 magnetic resonance spectroscopy and electron microscopy in chronic ductopenic rejection of human liver allografts. Gut 1998;42:735–743.
66. van Wassenaer-van Hall HN, van der Grond J, van Hattum J, Kooijman C, Hoogenraad TU, Mali WP. 31P magnetic resonance spectroscopy of the liver: correlation with standardized serum, clinical, and histological changes in diffuse liver disease. Hepatology 1995;21: 443–449.
67. Purvis LAB, Clarke WT, Pavlides M, Neubauer S, Robson MD, Rodgers CT. Does using a 16-element receive-array improve whole-liver 31P metabolite ratio quantification at 7T? In Proceedings of the 23rd Annual Meeting of ISMRM, Toronto, Canada, 2015. Abstract 0838.
68. Purvis LAB, Clarke WT, Pavlides M, Robson MD, Rodgers CT. 7T allows correct measurement of PDE in the human liver without decoupling In Proceedings of the 24th Annual Meeting of ISMRM, Singapore, 2016. Abstract 3961.

SUPPORTING INFORMATION

Additional Supporting Information may be found in the online version of this article

Table S1. List of Bloch simulation fitting steps for T_1 analysis.

Table S2. List of prior knowledge used for fitting the standard protocol. The phases of all peaks were additionally constrained to be the same as all the other peaks.

Table S3. Mean ± SD of ratios to total phosphate for 10 normal volunteers and 11 patients with cirrhotic livers from a 28min 3D CSI acquisition. Total phosphate was calculated as the sum of all visible peaks. The normal liver ratios are from the first volunteer scan. Significant differences between healthy and cirrhotic ratios are marked with stars: * $P < 0.05$, ** $P < 0.01$.

Fig. S1. The blue line shows the peak B_1^+ (i.e., with the coil at maximum voltage) for the $28 \times 27\,cm^2$ transmit loop calculated using the Biot-Savart law. The red x denote direct measurements of B_1 in the cube by repeated acquisition of FIDs with 4 ms excitation, 1500 ms T_R, 4 preparation scans and 4 averages followed by fitting using the phantom T_1 previously determined in fully relaxed inversion recovery experiments. The Biot-Savart calculated B_1^+ values are accurate to within 10%. This leads to $< 0.5\%$ error in saturation correction on a single peak, and $<1\%$ error on the reported concentrations.